Universal phase behaviors of intracellular lipid droplets

Shunsuke F. Shimobayashi[a,b,1] and Yuki Ohsaki[c]

[a]Department of Mathematical Science and Advanced Technology, Japan Agency for Marine-Earth Science and Technology, Yokohama 236-0001, Japan; [b]Department of Chemical and Biological Engineering, Princeton University, Princeton, NJ 08544; and [c]Department of Anatomy and Molecular Cell Biology, Nagoya University Graduate School of Medicine, Nagoya 466-8550, Japan

Edited by David A. Weitz, Harvard University, Cambridge, MA, and approved October 31, 2019 (received for review September 27, 2019)

Lipid droplets are cytoplasmic microscale organelles involved in energy homeostasis and handling of cellular lipids and proteins. The core structure is mainly composed of two kinds of neutral lipids, triglycerides and cholesteryl esters, which are coated by a phospholipid monolayer and proteins. Despite the liquid crystalline nature of cholesteryl esters, the connection between the lipid composition and physical states is poorly understood. Here, we present a universal intracellular phase diagram of lipid droplets, semiquantitatively consistent with the in vitro phase diagram, and reveal that cholesterol esters cause the liquid–liquid crystal phase transition under near-physiological conditions. We moreover combine in vivo and in vitro studies, together with the theory of confined liquid crystals, to suggest that the radial molecular alignments in the liquid crystallized lipid droplets are caused by an anchoring force at the droplet surface. Our findings on the phase transition of lipid droplets and resulting molecular organization contribute to a better understanding of their biological functions and diseases.

liquid crystal | lipid droplets | intracellular phase transition

Cholesterol is an essential component of cell membranes and its dysregulation leads to lethal diseases, such as arteriosclerosis and neurodegenerative disorders (1, 2). Cholesterol is inserted into cell membranes owing to its hydrophobicity upon uptake and modulates the physical interaction between phospholipids in cell membranes, which can cause liquid–liquid phase separation of a homogeneous lipid membrane into liquid-disordered (L_d) and liquid-ordered (L_o) phases (3–6). Some cholesterol is esterified and transported to lipid droplets (LDs), where it is stored as cholesteryl esters (CEs) (7). CEs are known to be cholesteric liquid crystals and undergo liquid–liquid crystal phase (L-LC) transition as a function of system parameters (e.g., temperature; refs. 8 and 9). Thus, CEs have the potential to induce the phase transition of LDs; however, the biophysics of the phase transition is poorly understood (10, 11).

To understand the L-LC transition in living cells, we cultured Huh7 cells (human hepatocarcinoma) with 170 μM cholesterol for 24 h. The methyl-β-cyclodextrin (MβCD) was used to dissolve hydrophobic cholesterol in hydrophilic culture medium (*Materials and Methods*). We observed the L-LC phase transition using polarized microscopy, which has been used to visualize liquid crystal phase (9) under near-physiological conditions while decreasing temperature (Fig. 1*A*). The temperature was controlled with a custom-made copper plate and thermoplate and probed by a thermocouple inserted into a dummy chamber filled with water. The phase transition temperature was different among LDs in each cell, which may be attributed to the mass ratio difference between CEs and triglicerides (TGs). Interestingly, many of the cells cultured with 170 μM cholesterol showed the coexistent states of liquid and liquid crystalline in a single LD at the intermediate temperature range (Fig. 1*A*). To statistically quantify the phase transition behavior, we counted as a function of temperature the probability that at least one LD in a single cell is at liquid crystalline state, p, with Huh7 cells ($n = 25$). Interestingly, the probability monotonically decreases as temperature increases for the Huh7 cells cultured with 25, 50, and 170 μM cholesterol (Fig. 1*C*), but, the slope is dependent on the added cholesterol concentration. At temperature (T) $T = 40°C$, almost all LDs were at L-phase ($p \approx 0$), but at $T = 10°C$, $p = 16$, 80, and 100% for 25, 50, and 170 μM cholesterol, respectively, indicating a clear correlation between the value of p and added cholesterol concentration. No LC LDs were observed even at $T = 10°C$ for the cells cultured with 400 μM oleic acid (OA) or only 10% FBS for 24 h.

Based on the statistical data, we next mapped an intracellular phase diagram as functions of temperature and the CE/TG mass ratio, M (Fig. 1*B*). To determine the CE/TG mass ratio, LDs were purified from cells and then the mass was measured by a thin-layer chromatography (TLC) assay (12–14) (SI Appendix, Fig. S1). The phase was determined to be L-phase if $0 \leqq p \leqq 50$ and LC-phase if $50 < p \leqq 100$. The phase diagram shows that LDs undergo the L-LC phase transition at the saturation mass ratio, $M^*(T)$, with a fixed temperature and that $M^*(T)$ decreases with a decrease in temperature. These findings suggest that CEs drive liquid crystallization of LDs.

We next investigated whether the phase transition phenomenon is universal for other types of cells. We cultured MEFs (mouse embryonic fibroblasts) and U2OS (human osteosarcoma) cells with 0.4 mM OA or only 10% fetal bovine serum (FBS) or 170 μM cholesterol for 24 h as we did with Huh7 cells. We never observed LDs with LC-phase for cells cultured

Significance

There is growing evidence suggesting that intracellular phase transitions play roles in biological functions. However, little is known about phase transitions of lipid droplets that are organelles involved in energy homeostasis. Here, we demonstrate a universal intracellular phase diagram of lipid droplets, consistent with the in vitro phase diagram, and reveal that cholesterol esters cause the liquid–liquid crystal phase transition under near-physiological conditions. We moreover combine in vivo and in vitro studies, together with the theory of confined liquid crystals, to suggest that the radial molecular alignments in the liquid crystallized lipid droplets are caused by an anchoring force at the droplet surface. These findings pave the way for a better understanding of their biological functions and diseases.

Author contributions: S.F.S. and Y.O. designed research; S.F.S. and Y.O. performed research; S.F.S. and Y.O. contributed new reagents/analytic tools; S.F.S. and Y.O. analyzed data; and S.F.S. wrote the paper.

The authors declare no competing interest.

This article is a PNAS Direct Submission.

[1]To whom correspondence may be addressed. Email: shimobayashi@jamstec.go.jp.

This article contains supporting information online at https://www.pnas.org/lookup/suppl/doi:10.1073/pnas.1916248116/-/DCSupplemental.

First published November 26, 2019.

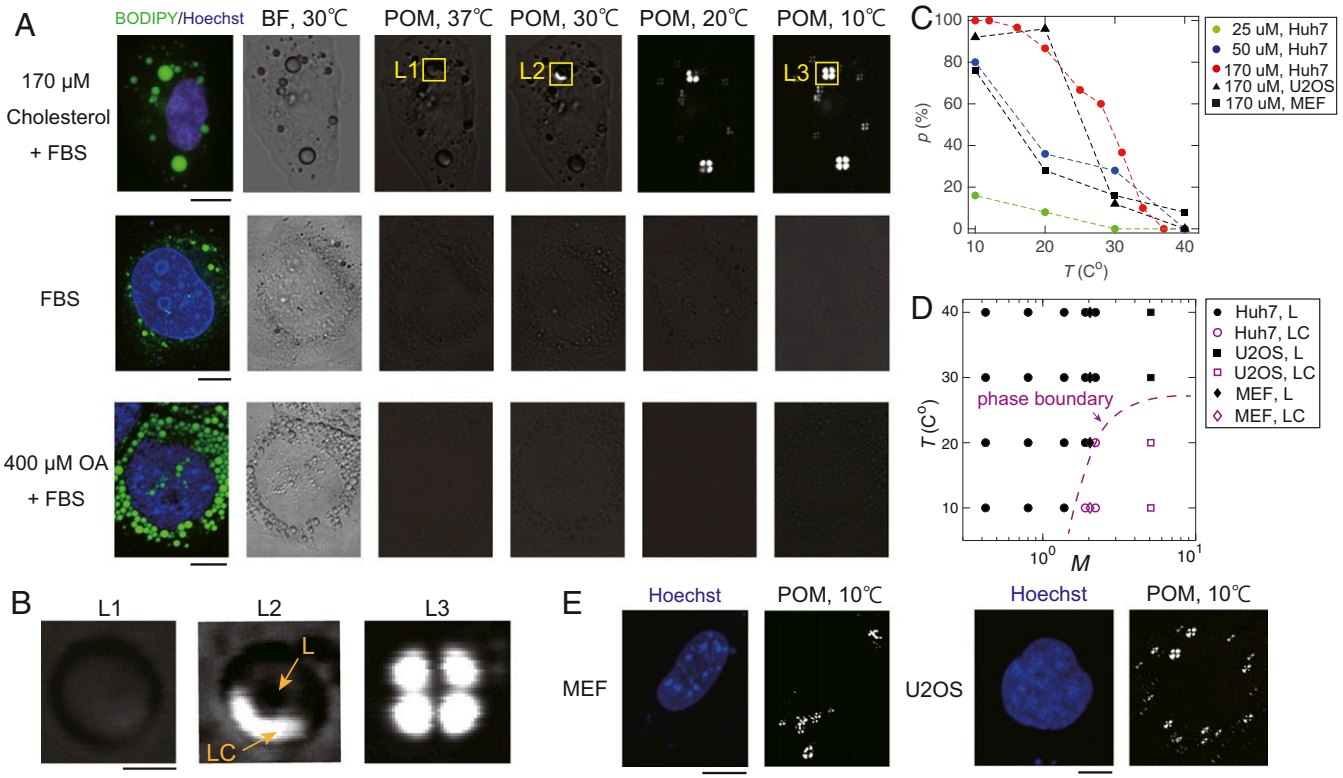

Fig. 1. (*A*) Optical images of live Huh7 cells for three different conditions (170 μM cholesterol, only 10% FBS, and 400 μM OA). BODIPY and Hoechst are markers of LDs and nucleus, respectively. The cross-polarized light was used for POM. BF, bright field; POM, polarized optical microscopy. (Scale bars, 10 μm.) (*B*) Phase transitions in an LD. From the left, liquid (L) phase (L1), the coexisting phase of liquid (L) and liquid-crystal (LC) phase (L2), and liquid-crystal (LC) phase (L3). (Scale bars, 2 μm.) (*C*) Probability that at least one LD is at liquid crystalline state, p, as a function of temperature, T, for various cell types and cultured conditions. $n = 25$. (*D*) Universal intracellular phase diagram as functions of T and CE/TG mass ratio, M. The phase was determined as L-phase if $0 \leqq p \leqq 50$ and LC-phase if $50 < p \leqq 100$. (*E*) Optical images of live MEF and U2OS cells cultured with 170 μM cholesterol for 24 h.

with 0.4 mM OA or only 10% FBS, but we observed LDs with LC-phase for MEF and U2OS cells cultured with 170 μM cholesterol as well as with Huh7 cells (Fig. 1*E*). These behaviors are consistent with the behaviors in Huh7 cells (Fig. 1*C*). The quantification of the CE/TG mass ratio for MEF and U2OS cells cultured with 170 μM cholesterol and overlay plot of the data points in intracellular phase diagram give us the universal phase boundary of L-LC phase transition in living cells, independent of cell types (Fig. 1*D*). The universal intracellular phase diagram confirms that CEs work as drivers of liquid crystallization of LDs.

To get quantitative insights into how CEs induce liquid crystal transition in LDs, we reconstituted artificial lipid droplets (ALDs) in vitro systems and studied the phase behavior (Fig. 2*A*). ALDs were reconstituted with cholesteryl oleates (COs) and/or trioleins (TOs), which are one type of typical CEs and TGs, respectively, and MilliQ (18.2 MΩ cm), to which the surfactant (DOPC, Brij58, or Tween20) was dissolved with 3 wt %. The surfactant solution was poured into COs which were preheated to $T = 70°C$ to liquidify, and it was immediately pipetted for emulsification and cooled down to room temperature ($T = 25 \pm 1°C$). This resulted in size-polydisperse ALDs with $R < 200$ μm, where R is the droplet diameter. Then, we mapped out the phase diagram of ALDs as functions of temperature T and the mole fraction of COs, ϕ_{co}. Note that $\phi_{co} = 0.5$ means equal mole amounts of COs and TOs. We here focused on the ALDs with $1 \leq R \leq 70$ μm and did not observe any size-dependent structure change; also, the phase transition temperature is independent of R and the type of surfactants (*SI Appendix*, Fig. S1). When the droplets were imaged under a polarized light microscope in the crossed Nicols condition, we observed three types of phases (i.e., L-phase, L-LC coexsiting phase, and LC-phase) (Fig. 2*B*). The droplets with $\phi_{co} = 1$ show L-LC phase transition at $T = 38 \pm 1$ °C. Observing the transition dynamics, the nucleation of LC-phase randomly occurs, implying homogeneous nucleation (Fig. 2*C* and Movie S1). Then, the molecules start radially aligning from the droplet surface, resulting in a transition from polydomain pattern to the pattern of the Maltese cross (Fig. 2*C*). On the other hand, the droplets with $\phi_{co} = 0$ are kept at the liquid state even at $T = 0 \pm 1°C$. Interestingly, the droplets with $0.2 \leq \phi_{co} \leq 0.8$ exhibit the L-LC coexistent phase. Observing the dynamics, the randomly nucleated LC droplets grow with a power law of approximately one-third while diffusing in a droplet, suggesting diffusion-limited Ostwald ripening (Movie S2) (15). We moreover realized that if the x axis of the phase diagram, that is, ϕ_{co}, is changed to the mass ratio using the molecular weights of COs and TOs (651.1 and 885.4 g/mol, respectively), interestingly the region we investigated in living cells (Fig. 1*D*) corresponds to the boxed region by the dashed line (Fig. 2*B*). We then found that the phase boundaries of both phase diagrams are semiquantitatively consistent (Figs. 1*D* and 2*B*). These findings suggest that LDs are a two-component system of CEs and TGs, and CEs drive the L-LC phase transition.

We next sought to understand why the molecules are radially aligned both in intracelluar LDs and ALDs with $\phi_{co} = 1$ and $R \leq 70$ μm below a certain phase transition temperature (Figs. 1*D* and 2*B*). Interestingly, we found that the ALDs with $\phi_{co} = 1$ and $R > 70$ μm did not show radial alignments but rather polydomain structure (Fig. 3 *A* and *B*). To get insights into the biophysics behind the radial alignment observed in the intracellular LDs (Fig. 1*B*), we studied why the size-dependent

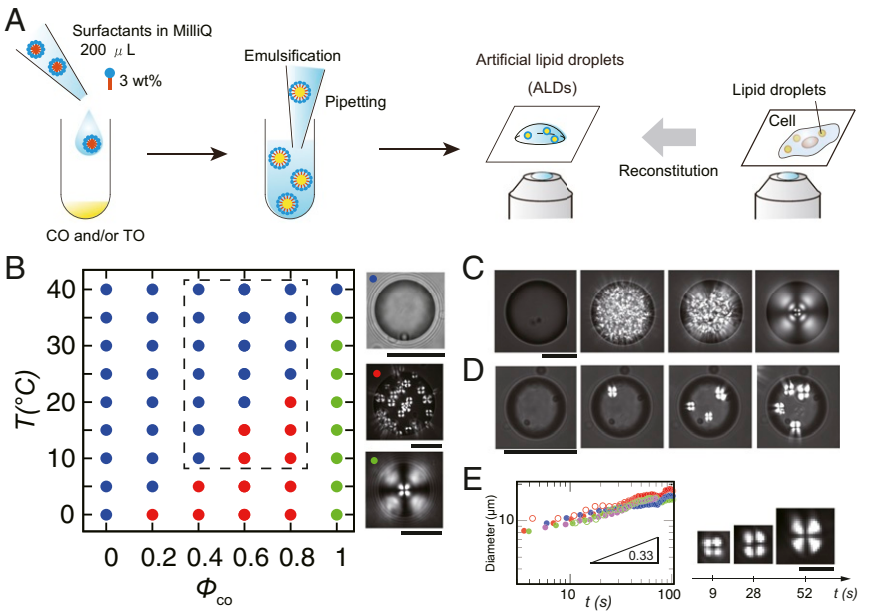

Fig. 2. Phase behavior of ALDs. (*A*) Schematic diagram of the experimental setup. (*B*) Phase diagram as functions of temperature *T* and mole fraction of COs, ϕ_{co}. The blue, green, and red circles represent the isotropic (L) phase, liquid-crystal (LC) phase, and the coexistent phase of liquid and liquid-crystal (L-LC), respectively. The region boxed by the dashed line corresponds to the investigated region in Fig. 1*D*. (*Right*) Typical images of three phases are presented. (Scale bars, 100 μm.) (*C*) Dynamics of the L-LC phase transition of an ALD with $\phi_{co} = 1$. (Scale bar, 100 μm.) (*D*) Dynamics of the L-LC phase transition of an ALD with $\phi_{co} = 0.6$. The LC-phase droplets nucleate and grow. (Scale bar, 100 μm.) (*E*) Growth of nucleated LC droplets. Different colors or markers represent different droplets (*Left*). Time sequence of a LC droplet (*Right*). (Scale bar, 10 μm.)

structure transition occurs. We first mapped out a phase diagram of the structure as functions of temperature T and diameter R (Fig. 3*B*). We increased the temperature to $T = 47 \pm 1$ °C above the L-LC phase transition temperature T_c (38 ±1 °C). All of the droplets above T_c were isotropic. The temperature was probed with an accuracy of ± 1.0°C using a thermocouple. Then, the temperature was decreased at a rate of −0.4°C/s to each point in the phase diagram. After about 10 min, the droplets were determined to be either in the radial-LC or polydomain-LC phase by means of cross-polarized light. The phase diagram clearly shows the structure transition between the radial and polydomain-LC phases in an all-or-none and size-dependent manner.

We next hypothesized from the phase diagram that the confinement of a part of the polydomain-LC droplet into a space with $R < 70$ μm induces the transition to the radial-LC phase. We aspirated a droplet with the polydomain-LC phase using a micropipette (internal diameter 60 μm) connected with a microinjector at $T = 25$°C and pinched out a small droplet with $R < R^*$ (Fig. 3*C*). Intriguingly, we found that the pinched drop with the radial-LC phase appears in the micropipet while the unpinched one remained the polydomain-LC phase (Movie S3). This finding suggests that the confinement to a spherical cavity with $R < R^*$ gives rise to the structure change to radial-LC phase. This is another piece of evidence for the size-dependent configuration transition.

To get physical insights into why the molecules in the intracellular LC droplets are radially aligned, we consider the physical mechanism behind the size-dependent structure transition by means of the theory of confined liquid crystals. Considering COs are in the smectic-A phase below $T \approx 38$°C (16), total free energy of the confined smectic-A phase is expressed as (9, 17–20)

$$F = \frac{1}{2}\int [K_{11}(\nabla \cdot \mathbf{n})^2 + B\gamma^2]dV + \frac{1}{2}\int W_0 \sin^2(\theta - \theta_0)\, dA. \quad [1]$$

The first term in Eq. **1** is the contribution of splay deformations, and K_{11} denotes the splay Frank elastic constant and controls the splay of the layer normal, where $\mathbf{n}$ is the local nematic director. The terms of twist $(K_{22}(\mathbf{n} \cdot \nabla \times \mathbf{n})^2)$ and bend $(K_{33}(\mathbf{n} \times \nabla \times \mathbf{n})^2)$ deformations considered in the free energy of the nematic phase are not present due to the layer constraint (9, 18, 19, 21). The second term is the energy associated with layer dilation, B is compression modulus, and $\gamma \equiv (d - d_0)/d_0$ is a relative change in layer thickness from its equilibrium value d_0 (18–20). The ratio of splay and Young constants determines a length scale $\lambda = \sqrt{K_{11}/B}$, which is close to smectic layer thickness. When the typical radius of curvature of the distorted SmA is much larger than $\lambda = \sqrt{K_{11}/B}$, the dilation term is decoupled from the curvature term and dropped from the equation (19). We therefore ignore this term. The third term is the surface anchoring energy, and θ_0 and θ are the preferred and actual anchoring angles, respectively. In our system, it is assumed that the anchoring energy is due to the physical interaction between cholesterol esters and phospholipids at the surface. Finally, our free energy is reduced to $F = \frac{1}{2}[\int K_{11}(\nabla \cdot \mathbf{n})^2 dV + \int W_0 \sin^2(\theta - \theta_0)\, dA]$, meaning that the free energy is the sum of the elastic energy in the droplet and anchoring energy at the surface.

Let us now compare free energies of the droplets with R between the radial-SmA phase and polydomain-SmA phase (denoted by $F_{\mathrm{rad}}(R)$ and $F_{\mathrm{poly}}(R)$, respectively). The gradient of the local nematic director, $\nabla \cdot \mathbf{n}$, in the radial-SmA phase is given by $\sim 1/R$ and total integrated Frank energy $F_{\mathrm{el,rad}}(R)$ is $(K_{11}/R^2)R^3 \sim K_{11}R$. On the other hand, $\nabla \cdot \mathbf{n}$ in the polydomain-SmA phase is $\sim 1/\xi$, where ξ is the correlation length of local nematic alignment (22). The elastic energy of each domain is $\sim K_{11}\xi$, and total integrated energy $F_{\mathrm{el,poly}}(R)$ is $\sim K_{11}\xi^{-2}R^3$. Assuming that $R \gg \xi$, the relation $F_{\mathrm{el,rad}}(R) \ll F_{\mathrm{el,poly(R)}}$ is obtained. Moreover, the droplet is coated by the amphiphile surfactant. The hydrophobic part that faces toward the droplet center gives rises to the strong homeotropic anchoring on the nematic director at the droplet surface (23). This

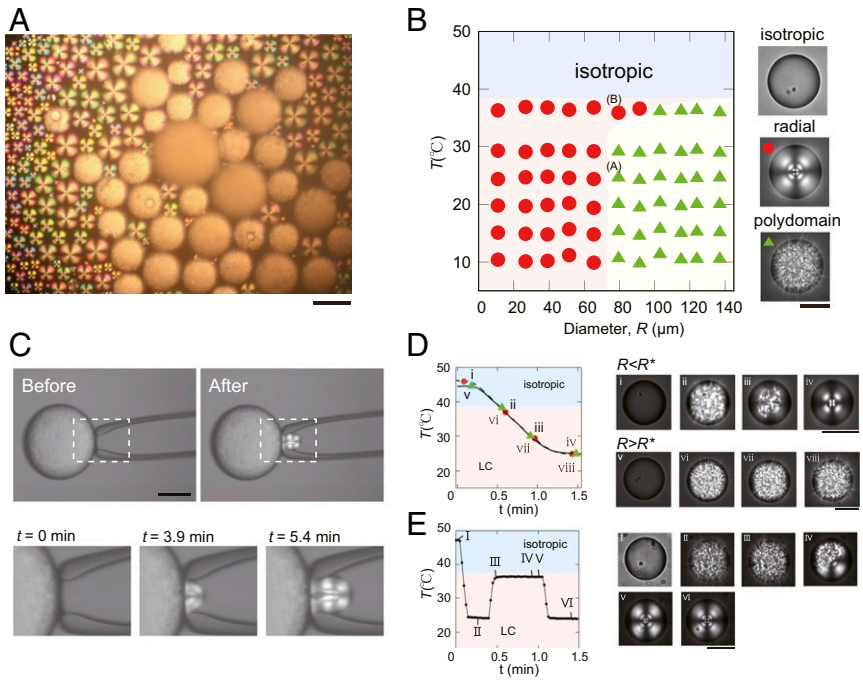

Fig. 3. Size-dependent structure transition of ALDs with $\phi_{co} = 1$. (*A*) An optical image of ALDs with crossed-polarizing light at $T = 25 \pm 1°C$. (Scale bar, 100 μm.) (*B*) Phase diagram as functions of temperature *T* and droplet diameter *R*. Red filled circles represent the radial-LC phase, where the molecules are radially aligned. Green filled triangles denote the polydomain-LC phase, where the molecules are aligned with a random direction in each domain. (*C*) Structure transition of ALDs with $\phi_{co} = 1$ confined to a spherical cavity. (*Top*) Polarized light microscopy images before (*Left*) and after (*Right*) micropipette aspiration are shown. (*Bottom*) Sequential images (*t*= 0, 3.9, and 5.4 min, from left to right) of the rectangular region in top images under a constant pressure. (Scale bars, 100 μm.) (*D*) Kinetic pathways of the isotropic-LC phase transition for two different sizes of droplets. (*Left*) Temperature change as a function of time *t*. (*Right*) Sequential polarized images for two pathways. (Scale bars, 50 μm.) (*E*) Structure transition from the polydomain-LC to radial-LC phase during temperature cycle experiments. (*Left*) Temperature change as a function of time *t*. (*Right*) Sequential polarized images. (Scale bar, 50 μm.)

situation can lead to $F_{anc,rad} \leq F_{anc,poly}$, where $F_{anc,rad}$ and $F_{anc,poly}$ are the anchoring energies for the radial-SmA and polydomain-SmA phases, respectively.

Finally, the relation $F_{rad}(=F_{el,rad} + F_{anc,rad}) \ll F_{poly}(= F_{el,poly} + F_{anc,poly})$ is obtained, suggesting that the polydomain Sm-phase is energetically unstable, independent of the droplet size. Observing the two kinetic pathways of the L-LC phase transition of droplets above or below R^*, the polydomain structure emerges on both pathways immediately after T passed through T_c (Fig. 3*D* and Movies S4 and S5). Then, the radial alignment starts only for the droplets with $R < R^*$. We therefore conclude that the polydomain phase is a kinetically trapped metastable state.

Moreover, we experimentally investigated whether the polydomain-SmA phase is metastable. We first prepared the droplet with $R \approx 80$ μm in the isotropic phase at $T = 47 \pm 1$ °C and decreased the temperature to $T = 24 \pm 1$ °C at a rate of -0.4°C/s (Fig. 3*B*, A), resulting in emergence of the polydomain-SmA phase (Fig. 3*E* and Movie S6). The temperature was then increased to $T = 36 \pm 1$ °C at the same rate (Fig. 3*B*, B) while the phase boundary was crossed between the two phases. Immediately, the radial alignment started from the droplet interface, leading to transition to the radial-SmA phase (Fig. 3*E*). Even if the temperature was returned to $T = 25 \pm 1°C$, the radial-SmA phase remained stable. These results provide evidence that the polydomain-SmA phase is the metastable state.

We now consider why the metastable polydomain Sm-phase undergoes the transition to the radial-Sm phase only for the droplets with $R < R^*$. Looking at the free-energy functional of the LC droplets (Eq. **1**), the driving force to overcome the volumetric elastic energy should come from the surface anchoring. The free energy gain due to the favorable surface anchoring corresponds to $\sim W_0 R^2$ and the structure transition to the radial-SmA phase should take place when the energy gain $\sim W_0 R^2$ overcomes the elastic energy $F_{el,poly} \sim K_{11} \xi^{-2} R^3$. Therefore, the threshold droplet diameter R^* is obtained as

$$R^* \sim \frac{W_0}{K_{11}} \xi^2. \quad [2]$$

In addition, ξ can be written as $\sqrt{R^* K_{11}/W}$ and estimated to be on the order of 1 μm with typical values for $K_{11} \sim 10^{-11}$ N (18, 23, 24), $W_0 \sim 10^{-4}$ J/m^2 for the "strong anchoring" (17, 25), and $R^* \approx 70$ μm. The ξ-value is comparable with the value observed in liquid crystalline polymers and elastomers (22) and is consistent with the optical observations (Fig. 3*B*). We conclude that the radial alignments for the droplets with $R < R^*$ are driven by the homeotropic anchoring force at the droplet surface and suggest that the radial alignments in LDs in living cells are caused by the anchoring force at the droplet surface (Fig. 1).

We also found that R^* remained constant at ~70 μm below $T \lesssim 30$ °C; on the other hand, R^* increased as T approached T_c and reached ~100 μm at $T = 36 \pm 1°C$ (Fig. 3*B*). We theoretically consider the mechanism behind the temperature dependence of R^*. As depicted in Eq. **2**, R^* is determined by the balance between W_0, K_{11}, and ξ. Elastic constant K_{11} has a second order in the nematic order parameter Q and W_0 is linear power of Q (23), leading to $W_0/K_{11} \sim Q^{-1}$. On the other hand, ξ experimentally seems to be constant so that the temperature dependence of ξ is likely minor in our experiments. Therefore, because $Q \to 0$ as $T \to T_c$, $R^* = W_0/K_{11}$ diverges as $T \to T_c$. In other words, the relative contribution of the surface alignment increases as $T \to T_c$. Also, R^* remained constant below

$T \sim 30\,^{\circ}$C; this would be attributed to the near-saturation of the Q value when $T \ll T_c$ (26).

There is a mounting evidence that phase transitions play important roles in living cells, particularly associating with membraneless organelles or condensates (3, 15, 27–29); nevertheless, there has been little work on the phase transition in LDs (30). Our study to quantify the universal intracellular phase diagram, semiquantitatively consistent with the in vitro phase diagram, is only the beginning of the fundamental biophysics for LDs. We moreover combine in vivo and in vitro studies, together with the theory of confined liquid crystals, to suggest that the radial molecular alignments in LDs in living cells are caused by the anchoring force at the droplet surface. However, it is still unclear whether the radial alignments cover the whole droplet or only near the LD surface and whether the internal structure can be involved in physiological functions of LDs, as discussed about LDs or LDL for several decades (10, 31–36). Daum and coworkers (32) studied the LD structure in yeast cells by using differential scanning calorimetry and small-angle X-ray scattering and observed a lamellar structure with a repeat distance of 3.7 nm for steryl ester (SE)-rich LDs below a certain physiological temperature. They moreover proposed a model in which a liquid TG core is surrounded by shells of SE (32). More recently, Baumesiter and coworkers (33) revealed with cryo-transmission electron microscopy that LDs in mammalian cells have a core-shell organization of an amorphous interior and a shell with lattice spacing of 3.4 to 3.6 nm under certain cycle stages or metabolic scenarios, and such features disappear with a heat shock of 43°C. These previous reports have implied that the phase change is driven by the temperature and lipid composition (10, 31–36); however, there has been a lack of comprehensive understanding of phase behaviors of LDs.

In the current study, we map out the intracellular phase diagram as a function of temperature and CE/TG mass ratio, consistent with the in vitro phase diagram, and observed the universal phase boundary of the L-LC phase transition by a combination of biochemical methods and polarized imaging. We can safely conclude from our findings that the liquid crystalline nature of CEs universally determines the intracellular phase behaviors of LDs. The structural details may be revealed by the investigation of the same LDs using multiple techniques including polarized optical microscopy and cryo-electron microscopy and the comparison between in vivo and in vitro LDs in the future. Such a deeper understanding of the LD structure will contribute to biological functions and diseases on LDs. For example, macrophages that are highly loaded with CEs can cause the lipid ordering in LDs and differentiate to foam cells; these cells are the main cellular components of fatty streaks and indicate the earliest stage of atherosclerosis (10, 11). Investigation of the relation between the structure change due to the L-LC transition and the onset of differentiation to foam cells might give us novel insights into the mechanism behind arteriosclerosis.

Materials and Methods

The Cell Line. Huh7 cell lines were obtained from the Japanese Collection of Research Bioresources Cell Bank. MEF and U2OS were kindly donated by Noboru Mizushima, Tokyo University, Tokyo and Hidemasa Goto, Aichi Cancer Center, Aichi, Japan, respectively. Cells were cultured in minimum essential medium (for Huh7) or Dulbecco's modified Eagle's medium (for other cells) supplemented with 10% of FBS and antibiotics at 37°C in a humidified atmosphere of 95% air and 5% CO_2. In some experiments, the cells were cultured at a certain concentration of OA (Sigma-Aldrich) in complex with fatty acid-free bovine serum albumin (Wako) at a molar ratio of 6:1. In other experiments, the cells were cultured at a certain concentration of cholesterol (Sigma-Aldrich) in complex with methly-β-cyclodextrin (Sigma-Aldrich) at a molar ratio of 1:6.

LD Purification and TLC Assay. The LD fraction was purified by nitrogen cavitation and sucrose density ultracentrifugation as described before (14). Lipids were extracted (12) and separated on HPTLC Silica gel 60 (Merck) with hexane:diethylether:acetic acid (80:20:1) and charred by 3% copper acetate in 85% phosphoric acid at 180 °C.

Microscopy and Imaging. Polarized light imaging was performed under an inverted microscope (Nikon Ti-E) with a confocal laser scanning system (Nikon A1), equipped with a ×4, 0.13 N.A., ×10, 0.45 N.A., and ×20, 0.75 N.A. dry objective lens (Nikon, Japan). The images were captured by a Andor iXon3 EM-CCD camera or Canon NY-X6i colored camera.

Micromanipulation. This procedure was performed using a Narishige micromanipulator (MM-92) and pneumatic microinjector (IM-11-2) mounted on an inverted microscope (Nikon Ti-E), equipped with a glass micropipette (60-μm internal diameter; VacuTip FCH; Eppendorf).

Temperature Control and Logging. Temperature was controlled by means of a custom-made copper plate with a thickness of 200 μm mounted on a thermo-plate (CHSQ-C; Tokai Hit). The copper plate had a hole of 4 mm in diameter at the center. The temperature was probed by a thermocouple inserted into a dummy chamber filled with water and was logged.

All data are included in the manuscript and *SI Appendix*.

ACKNOWLEDGMENTS. We thank T. Fujimoto (Juntendo University), E. M. Terentjev (University of Cambridge), J. Fukuda (Kyushu University), and P. J. Ackerman and C. Choi (Princeton University) for fruitful discussions. We wish to acknowledge the Division for Medical Research Engineering, Nagoya University Graduate School of Medicine for technical support of microscopes. This work was supported by Japan Society for the Promotion of Science KAKENHI (grant 18K13521 to S.F.S. and grant 18K06829 to Y.O.) and a Sasakawa Scientific Research Grant from The Japan Science Society (2018-4022 to S.F.S.).

1. K. J. Rayner *et al.*, MiR-33 contributes to the regulation of cholesterol homeostasis. *Science* **328**, 1570–1573 (2010).
2. J. E. Vance, Dysregulation of cholesterol balance in the brain: Contribution to neurodegenerative diseases. *Dis. Model. Mech.* **5**, 746–755 (2012).
3. S. F. Shimobayashi, M. Ichikawa, T. Taniguchi, Direct observations of transition dynamics from macro- to micro-phase separation in asymmetric lipid bilayers induced by externally added glycolipids. *Europhys. Lett.* **113** , 56005 (2016).
4. S. L. Veatch, S. L. Keller, Miscibility phase diagrams of giant vesicles containing sphingomyelin. *Phys. Rev. Lett.* **94**, 148101 (2005).
5. T. Hamada, R. Fujimoto, S. F. Shimobayashi, M. Ichikawa, M. Takagi, Molecular behavior of DNA in a cell-sized compartment coated by lipids. *Phys. Rev. E Stat. Nonlinear Soft Matter Phys.* **91**, 062717 (2015).
6. T. Baumgart, S. Hess, W. Webb, Imaging coexisting fluid domains in biomembrane models coupling curvature and line tension. *Nature* **425**, 821–824 (2003).
7. Y. Ohsaki, M. Suzuki, T. Fujimoto, Open questions in lipid droplet biology. *Chem. Biol.* **21**, 86–96 (2014).
8. J. Planer, Notiz über das cholestearin. *Annalen der Chemie und Pharmacie* **118**, 25–27 (1861).
9. P. G. de Gennes, J. Prost, *The Physics of Liquid Crystals* (Oxford University Press, New York, 1995).
10. A. T. Lada, M. C. Willingham, R. W. St Clair, Triglyceride depletion in THP-1 cells alters cholesteryl ester physical state and cholesterol efflux. *J. Lipid Res.* **43**, 618–628 (2002).
11. G. Bautista *et al.*, Polarized thg microscopy identifies compositionally different lipid droplets in mammalian cells. *Biophys. J.* **107**, 2230–2236 (2014).
12. E. Bligh, W. Dyer, A rapid method of total lipid extraction and purification. *Can. J. Biochem. Phys.* **37**, 911–917 (1959).
13. M. Suzuki *et al.*, Derlin-1 and UBXD8 are engaged in dislocation and degradation of lipidated ApoB-100 at lipid droplets. *Mol. Biol. Cell* **23**, 800–810 (2012).
14. T. Fujimoto, H. Kogo, K. Ishiguro, K. Tauchi, R. Nomura, Caveolin-2 is targeted to lipid droplets, a new "membrane domain" in the cell. *J. Cell Biol.* **152**, 1079–1085 (2001).
15. S. C. Weber, M. Haataja, J. Berry, C. P. Brangwynne, N. Vaidya, RNA transcription modulates phase transition-driven nuclear body assembly. *Proc. Natl. Acad. Sci. U.S.A.* **112**, E5237–E5245 (2015).
16. D. H. Croll, D. M. Small, J. A. Hamilton, Molecular motions and thermotropic phase behavior of cholesteryl esters with triolein. *Biochemistry* **24**, 7971–7980 (1985).
17. J. H. Erdmann, S. Umer, J. W. Doane, Configuration transition in a nematic liquid crystal confined to a small spherical cavity. *Phys. Rev. Lett.* **64**, 1907–1910 (1990).
18. J. B. Fournier, G. Durand, Focal conic faceting in smectic-A liquid crystals. *J. Phys. II* **1**, 845–870 (1991).
19. Y. H. Kim, D. K. Yoon, H. S. Jeong, O. D. Lavrentovich, H. T. Jung, Smectic liquid crystal defects for self-assembling of building blocks and their lithographic applications. *Adv. Funct. Mater.* **21**, 610–627 (2011).
20. C. Blanc, M. Kléman, Curvature walls and focal conic domains in a lyotropic lamellar phase. *Eur. Phys. J. B* **10**, 53–60 (1999).
21. D. Lavrentovich, Hierarchy of defect structures in space filling by flexible smectic-A layers. *Sov. Phys. JETP* **64**, 984–990 (1987).
22. S. V. Fridrikh, E. M. Terentjev, Polydomain-monodomain transition in nematic elastomers. *Phys. Rev. E* **60**, 1847–1857 (1999).

23. E. M. Terentjev, Stability of liquid crystalline macroemulsions. *Europhys. Lett.* **32**, 607–612 (1995).
24. O. D. Lavrentovich, Topological defects in dispersed liquid crystals, or words and worlds around liquid crystal drops. *Liq. Cryst.* **24**, 117–125 (1998).
25. A. Mertelj, M. Čopič, Surface-dominated orientational dynamics and surface viscosity in confined liquid crystals. *Phys. Rev. Lett.* **81**, 5844–5847 (1998).
26. M. L. Magnuson, B. M. Fung, J. P. Bayle, On the temperature dependence of the order parameter of liquid crystals over a wide nematic range. *Liq. Cryst.* **19**, 823–832 (1995).
27. C. P. Brangwynne *et al.*, Germline P granules are liquid droplets that localize by controlled dissolution/condensation. *Science* **324**, 1729–1732 (2009).
28. M. Feric *et al.*, Coexisting liquid phases underlie nucleolar subcompartments. *Cell* **165**, 1686–1697 (2016).
29. D. Bracha *et al.*, Mapping local and global liquid phase behavior in living cells using photo-oligomerizable seeds. *Cell* **175**, 1467–1480 (2018).
30. A. R. Thiam, R. V. Farese Jr, T. C. Walther, The biophysics and cell biology of lipid droplets. *Nat. Rev. Mol. Cell Biol.* **14**, 775–786 (2013).
31. M. Pregetter *et al.*, Microphase separation in low density lipoproteins. *J. Biol. Chem.* **274**, 1334–1341 (1999).
32. T. Czabany *et al.*, Structural and biochemical properties of lipid particles from the yeast Saccharomyces cerevisiae. *J. Biol. Chem.* **283**, 17065–17074 (2008).
33. J. Mahamid *et al.*, Liquid-crystalline phase transitions in lipid droplets are related to cellular states and specific organelle association. *Proc. Natl. Acad. Sci. U.S.A.* **116**, 16866–16871 (2019).
34. G. S. Ginsburg, D. M. Small, D. Atkinson, Microemulsions of phospholipids and cholesterol esters. Protein-free models of low density lipoprotein. *J. Biol. Chem.* **257**, 8216–8227 (1982).
35. R. J. Decklebau, G. Graham Shipley, D. M. Small, Structure and interactions of lipid in human plasma low density lipoproteins. *J. Biol. Chem.* **252**, 744–754 (1977).
36. V. Kumar *et al.*, Three-dimensional cryoEM reconstruction of native LDL particles to 16å resolution at physiological body temperature. *PLoS One* **6**, e18841 (2011).